Article

Cu/Mn Synergy Catalysis-Based Colorimetric Sensor for Visual Detection of Hydroquinone

Ningning Xing [1], Lilin Yang [2], Li Wang [1], Yanxiang Lu [1], Hongkun Zhang [1], Xijun Sun [1], Min Zhao [3], Wenjie Tan [1,*] and Jie Yang [4,*]

[1] School of Material Science and Engineering, Shandong Jianzhu University, Jinan 250022, China; xingningning@sdjzu.edu.cn (N.X.); wangli09012023@163.com (L.W.); lyx040419@163.com (Y.L.); zhanghongkun2004@163.com (H.Z.); ffhlz321@163.com (X.S.)
[2] Shandong Jiazihu New Material Technology Co., Ltd., Jinan 250022, China; yanglilin2019@163.com
[3] School of Foreign Languages, University of Jinan, Jinan 250024, China; zhaomin0632@126.com
[4] Department of Pharmaceutical and Bioengineering, Zibo Vocational Institute, Zibo 255000, China
* Correspondence: tanwenjie19@sdjzu.edu.cn (W.T.); yangjie715@yeah.net (J.Y.)

Abstract: The reliable detection of environmental contaminants can correctly forecast the degree of environmental pollution that has occurred, which contributes to improving the environmental purification rate and maintaining the ecological balance. Herein, a novel hierarchical biomimetic catalysis MnO_2@CuAl-CLDHs was designed and synthesized using a facile method, which exhibited significantly enhanced peroxidase-like activity due to the unique composition and hierarchical mesoporous structure. Under optimized operational conditions, a visible colorimetric array based on the superior nanozyme activity of MnO_2@CuAl-CLDHs was developed for the quantitative determination of hydroquinone with a wide linear detection range (1–100 μM) and a low detection limit (0.183 μM). Simultaneously, our presented strategy could analyze hydroquinone in real water samples with high accuracy. Therefore, the bimetallic co-catalyzed nanozymes are expected to be the perfect replacement for natural enzymes to develop convenient and efficient sensors.

Keywords: MnO_2@CuAl-CLDHs; nanozyme; catalytic; colorimetric detection; hydroquinone

1. Introduction

The small organic molecules of hydroquinone (HQ) are widely used in pharmaceutical, dyes, pesticides, and plastics areas [1,2]. HQ has not only brought economic benefits for society, but also made an impact on the environment and human health. According to the U.S. Environmental Protection Agency (EPA), the excessive emission of HQ (3.5 mg/L) is harmful to human health due to its high toxicity and the difficulty of degradation, which can cause fatigue, tachycardia, hepatic injury, impairment of the kidney, and even death [3,4]. Therefore, the sensitive detection for HQ in water is of great importance. In recent years, various analytical methods have been developed for the detection of HQ, such as spectrophotometry [5], electrochemical techniques [6], high-performance liquid chromatography [7], atomic absorption spectroscopy (AAS) [5], fluorescence [8], etc. However, these traditional instrumental analysis methods are complex in equipment and operation, have a high cost, and are time-consuming. Therefore, it is imperative to develop a rapid analysis method with outstanding sensitivity for HQ.

The colorimetric method is a good candidate for the visual detection of environmental contaminants without expensive instruments. However, the key challenge of colorimetric assays is choosing a specific catalyst to effectively oxidize the chromogenic substrate and produce a significant color change. Natural enzymes with high catalytic activity and substrate specificities are excellent catalysts for colorimetric sensing [9]. The mild reaction conditions are the prerequisite for efficient catalysis of natural enzymes. Moreover, their wide range of applications faces various challenges, such as harsh reaction conditions,

easy inactivation, complex purification process, and high cost [10–12]. In order to overcome the shortcomings of natural enzymes, it is desirable to design enzyme substitutes with high activity, high stability, and a low cost. In 1990s, researchers found that some nanomaterials exhibited catalytic activities similar to natural enzymes, and then the term "nanozyme" was coined by Scrimin's team in 2004 [13]. Then, in 2007, Yan et al. first discovered that Fe_3O_4 reacted with peroxidase substrates and speculated that nano Fe_3O_4 had a catalytic activity similar to the nature of peroxidase, which was confirmed by systematic comparison of catalytic efficiency and enzymatic kinetic between Fe_3O_4 and natural peroxidase [14]. Nanozymes based on nanomaterials are the next-generation artificial enzymes with enzyme-like characteristics and have been applied in colorimetric assays to catalyze the chromogenic substrates [15]. In addition, synthetic nanozymes possess significant advantages of structural diversity, catalytic activity tunability, and easy storage, which provide a new opportunity for the development of colorimetric sensing in the field of environmental protection.

Generally, enzyme-like activities of nanozymes mainly include catalase, peroxidase, oxidase, superoxide dismutase, etc., and peroxidase is a hotspot for research and application. Some common nanomaterials such as metal nanoparticles (Au, Ag, Pt, Pd), metal oxides (Fe_3O_4, Cu_2O, CeO_2, V_2O_5, MnO_2), carbon materials (graphene, carbon nanotubes, and carbon nanodots), and so on have been reported to possess excellent enzymatic catalytic activity. Among them, manganese-based oxides (Mn-O) have been shown to possess outstanding peroxidase and oxidase-mimicking activities due to the variation of the valence and rapid electron transfer of Mn ion [16]. Most manganese-based oxide nanozymes are two-dimensional (2D) nanosheets with the advantages of large surface areas and abundant active sites, but they are prone to conglomerate easily and can lead to the active sites being covered, which reduces the catalytic activity. Therefore, increasing the dispersity of two-dimensional nanozymes is one of the effective ways to improve its catalytic activity. In addition to exploring various synthesis methods, building composites with other materials is a simple and effective way to avoid the agglomeration of 2D nanomaterials and expose more active sites [17,18].

Layered double hydroxide (LDHs) as a hydrotalcite-like multifunctional material possesses a sandwich structure and the guest layer consists of anions sandwiched between the positively charged main layers. Due to the advantages of high chemical and structure stability, flourishing pore structure, large specific surface area, and simple preparation process, the LDHs are widely used as catalysts or catalyst carriers [19,20]. The ideal LDHs structure can achieve the attachment of 2D nanomaterials through electrostatic interaction or in situ growth to construct a composite with abundant pores. Simultaneously, the surface electron distribution and geometric construction of the composite are regulated by confined pore canals, which will affect the activity of the catalysts. The crystal phase of LDHs will decompose under 500–600 °C to form calcined LDHs (CLDHs) with a new crystal structure, which has excellent structural memory properties, greater thermal stability, and highly exposed active sites. Additionally, compared with other metals, the presence of copper-based nanomaterials can effectively enhance the overall catalytic activity of the composite catalysts because the Cu^+ of low valence can accelerate the electron transfer on the catalyst surface [21,22]. It has been reported that the synergistic effect between Cu-based and Mn-based composites can improve chemical catalytic activity [23–25]. However, the research on the application of Cu-based LDHs sensors for contamination detection in water is rarely studied, especially in the integration of Cu-based, LDHs-derived nanocomposites (such as Cu-based CLDHs) with mangan-based oxides. Therefore, the incorporation of Cu-based LDHs with 2D mangan-based oxides such as MnO_2 has the potential to become the ideal way to build high-active nanozyme.

Taking advantage of convenient operation and visual detection, the colorimetric sensor based on nanozymes has been widely used in environment contamination analysis. Herein, we designed and fabricated a novel hierarchical flower-like MnO_2@CuAl-CLDHs through a facile hydrothermal calcination method. The as-prepared MnO_2@CuAl-CLDHs

exhibited excellent peroxidase-like activities due to the synergistic effect between Cu and Mn ions, which could catalyze the oxidation of colorless TMB into blue oxTMB in H_2O_2. Subsequently, with the addition of reductive HQ into the chromogenic system, the blue oxTMB was quickly reduced into colorless TMB through the electron transfer; thus, a visual colorimetric sensor for HQ determination in water was constructed with high sensitivity. The synergistic effects of MnO_2@CuAl-CLDHs nanozyme led to a relatively low detection limit (LOD) of 0.183 μM for HQ. In addition, the super selectivity and reusability allowed MnO_2@CuAl-CLDHs to have a high economic value in real-world applications.

2. Materials and Methods

2.1. Regents and Materials

$Cu(NO_3)_2·3H_2O$ (AR, 99%), $Al(NO_3)_3·9H_2O$ (AR, 99%), 3,3′,5,5′-tetramethylbenzidine (TMB, 98%) and isopropanol (IPA, AR, ≥99.7%) were all provided by Aladdin Reagent Co., Ltd. (Shanghai, China). Dimethyl sulfoxide (DMSO, ACS, ≥99.9%), urea (AR, 99%), $KMnO_4$, and sodium azide (NaN_3, ≥99%) were all obtained from Sinopharm Chemical Reagent Co., Ltd. (Shanghai, China). Hydrogen peroxide (H_2O_2, 30%) was purchased from Yantai Far East Fine Chemical Co., Ltd. (Yantai, Shandong, China). p-benzoquinone (BQ, 99%) was procured from Shanghai Macklin Biochemical Technology Co., Ltd. (Shanghai, China). All reagents were used without further purification before use.

2.2. Characterization

X-ray diffraction (XRD) patterns of samples were obtained by an X-ray diffractometer (Bruker D8, badensko-wuertembersko, Karlsruhe, Germany). The morphology of samples was characterized by field-emission scanning electron microscopy, equipped with an energy dispersive X-ray spectrometer (EDS) (FESEM, ZEISS G500, Jena, Thuringia, Germany). The lattice fringe of samples was performed by transmission electron microscopy (TEM, FEI Talos F200S, Waltham, MA, USA). The chemical properties and composition of the sample were identified by X-ray photoelectron spectroscopy (XPS, ESCALAB Xi+, East Grinstead, UK). The N_2 adsorption-desorption isotherm was measured by a physisorption analyzer (ASAP2020M+C, Micrometric, Atlanta, GA, USA) and the specific surface area of the material was measured by multipoint BET (Brunauer, Emmett and Teller) method, while the pore size distribution was estimated by the Barrett–Joyner–Halenda (BJH) method. The absorbance of the reaction system was recorded by a UV-vis spectrophotometer (UV-vis spectrophotometer). The electron paramagnetic resonance (EPR) spectra were tested by an EPR spectrometer (Bruker EMXnano, Baden-Württemberg, Karlsruhe, Germany).

2.3. Synthesis of Flower-like MnO_2@CuAl-CLDHs

The CuAl-CLDHs were prepared via hydrothermal reaction and calcination. Typically, 15 mL DMSO and 35 mL deionized water were evenly mixed to obtain a component solvent. Subsequently, 9 mmol $Cu(NO_3)_2·3H_2O$, 4.5 mmol $Al(NO_3)_3·9H_2O$, and 12 mmol urea were added into the mixed solvent (in order) under the magnetic stirrer for 15 min. After the complete dissolution of the above solution, the mixture was filled into a Teflon-lined, stainless-steel autoclave, which was kept at 110 °C for 12 h. The bright blue solid products obtained by centrifugation (6000 rpm, 3 min) were washed three times with deionized water and ethanol, respectively, and then dried at 100 °C for 24 h. Finally, the dried products were calcined at 500 °C for 1 h under air atmosphere at a heating rate of 5 °C/min. The as-prepared samples were denoted as CuAl-CLDHs.

The growth of MnO_2 nanosheets on the surface of CuAl-CLDHs was realized through the hydrothermal method. First, 0.4 mmol $KMnO_4$ was dissolved in 80 mL deionized water and stirred for 10 min. Then, 100 mg CuAl-CLDHs was added into the above solution and stirred for another 30 min to form the uniform mixture. Finally, the mixture was transferred into Teflon-lined, stainless-steel autoclave and heated at 140 °C for 6 h. After the reaction finished, the products were filtrated and washed three times with deionized water, and then dried at 60 °C for 12 h. The final products were denoted as MnO_2@CuAl-CLDHs.

2.4. Peroxide-like Activity of Flower-Like MnO₂@CuAl-CLDHs

The peroxidase-like activity (POD) of MnO$_2$@CuAl-CLDHs was monitored by the catalytic oxidation of TMB in the presence of H$_2$O$_2$. In brief, 100 μL of TMB (5 mM), 50 μL of MnO$_2$@CuAl-CLDHs (1 mg/mL), and 100 μL of H$_2$O$_2$ (20 mM) were added in 2.75 mL HAc-NaAc buffer (0.2 M, pH 4.0) to construct the colorimetric system, which was incubated at room temperature for 5 min. The UV-vis absorption spectrum of the colorimetric system was recorded ranging from 400 to 800 nm by the UV-vis spectrophotometer. In addition, the effects of pH (pH 3.0–8.0), incubation time (1–15 min), incubation temperature (10–60 °C), concentration of TMB (1–15 mM), H$_2$O$_2$ (5–35 mM), and catalyst (0.3–2.0 mg/mL) on the peroxidase-like activity of MnO$_2$@CuAl-CLDHs were investigated to optimize the enzyme-catalyzed reaction conditions.

Furthermore, the kinetic analysis with various concentrations of TMB (0.03–0.5 mM) and H$_2$O$_2$ (0.1–0.8 mM) as substrates was conducted in HAc-NaAc buffer (0.2 M, pH 4.0) containing MnO$_2$@CuAl-CLDHs (1.2 mg/mL). The absorbance of the reaction system at 652 nm was recorded by a UV-vis spectrophotometer using time scanning mode. The catalytic behavior of MnO$_2$@CuAl-CLDHs conformed to the Michaelis–Menten equation (Equation (1)). Then, the Lineweaver–Burk double reciprocal plots were used to calculate the Michaelis constant (K$_m$) and maximal reaction rate (V$_{max}$) (Equation (2)).

$$V_0 = \frac{V_{max}[S]}{(K_m + [S])} \tag{1}$$

$$\frac{1}{V_0} = \left(\frac{K_m}{V_{max}}\right) \times \left(\frac{1}{[S]}\right) + \frac{1}{V_{max}} \tag{2}$$

where V$_0$ stands for the initial velocity, [S] stands for the concentration of TMB or H$_2$O$_2$, V$_{max}$ stands for the maximal reaction velocity, K$_m$ stands for Michaelis constant.

2.5. Detection of HQ

The colorimetric assays for HQ were carried out based on the optimal enzyme-catalyzed reaction conditions. The detailed experimental procedures were as follows: 100 μL of TMB (7 mM), 50 μL of MnO$_2$@CuAl-CLDHs (1.2 mg/mL), and 100 μL of H$_2$O$_2$ (25 mM) were added in 2.75 mL HAc-NaAc buffer (0.2 M, pH 4.0) and incubated at 30 °C for 9 min. Then, 100 μL different concentrations (1–100 μM) of HQ were added to the above colorimetric system and the mixture was further incubated at 30 °C for another 5 min. The blue color of the colorimetric system slowly receded with the addition of reductive HQ, and the intensity of the absorption peak at 652 nm decreased gradually. Therefore, the concentration of HQ could be calculated by monitoring the change of absorbance at 652 nm with UV-vis spectrophotometer.

2.6. Reusability of MnO₂@CuAl-CLDHs

After repeated use, the reproducibility and stability of MnO$_2$@CuAl-CLDHs were studied according to the experimental procedures in Sections 2.4 and 2.5. MnO$_2$@CuAl-CLDHs were collected from the reaction solution by centrifugation and washed with distilled water for the next run. The MnO$_2$@CuAl-CLDHs, after being used five times, was characterized by SEM to evaluate the chemical and structural stability.
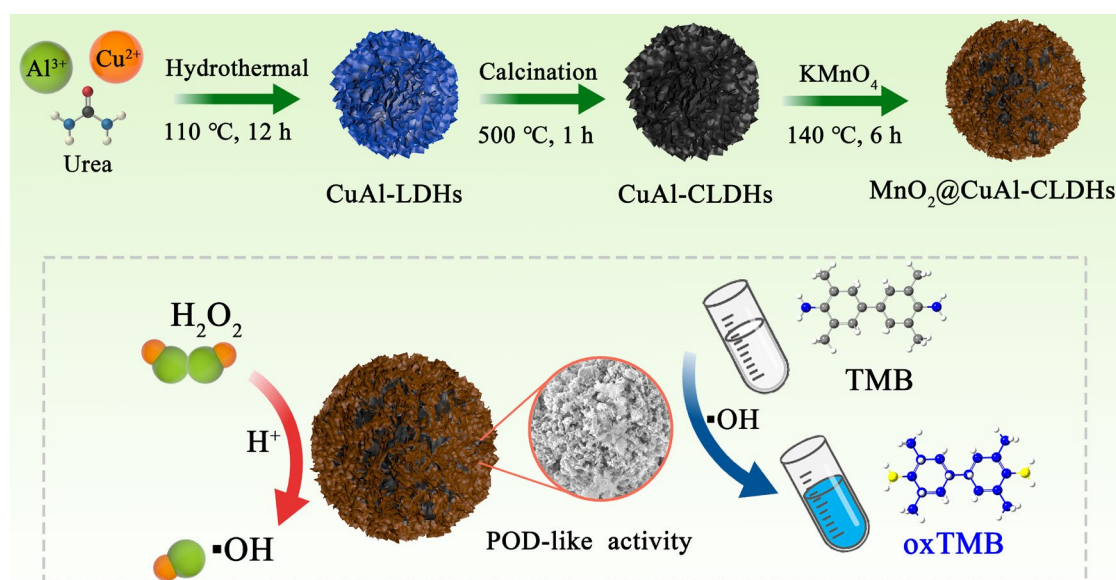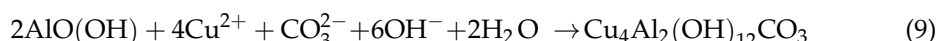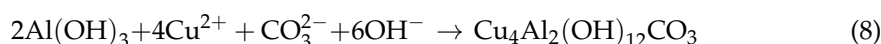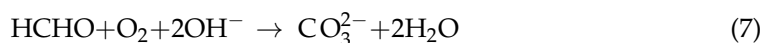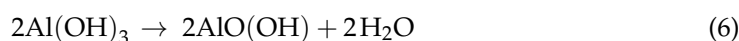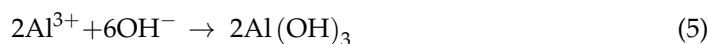
2.7. Analysis of HQ in Real Samples

In order to evaluate the practicability of the proposed colorimetric assay, the HQ in different water samples was detected. The real samples were mainly tap water and lake water, which came from the laboratory and Yingxue Lake (Shandong Jianzhu University). The above water samples were filtered with 0.22 μm filter membrane before use to remove the physical impurities. Finally, the concentrations of HQ in these water samples were detected and calculated by the above-mentioned colorimetric assay and the percent recovery values were obtained.

3. Results and Discussion

3.1. Design and Preparation of MnO₂@CuAl-CLDHs

The design and fabrication process of flower-like MnO$_2$@CuAl-CLDHs was shown in Scheme 1. Firstly, CuAl-LDHs microspheres were prepared by a facile hydrothermal method in which copper nitrate and aluminum nitrate were used as the metal source and urea was used as precipitant. The Cu^{2+} and Al^{3+} reacted with the anions slowly released from the urea to form 2D CuAl-LDHs nanosheets, which further self-assembled into flower-like microspheres. The formation mechanism of CuAl-LDHs was displayed as follows (Equations (3)–(9)). Subsequently, the CuAl-LDHs were decomposed into copper-aluminum bimetallic oxides via a high-temperature calcination process. Finally, the MnO$_2$ nanosheets were grown in situ on CuAl-LDHs surface to form 3D multi-order flower-like MnO$_2$@CuAl-CLDHs. The strong synergy between copper and manganese was conducive to enhancing the catalytic activities of as-synthesized composite, and realizing the visually sensitive detection for HQ.

$$6CO\left(NH_2\right)_2 + 6H_2O \rightarrow 6HCHO + 4NH_3 \tag{3}$$

$$NH_3 + H_2O \rightarrow NH_4^+ + 4OH^- \tag{4}$$

$$2Al^{3+} + 6OH^- \rightarrow 2Al\left(OH\right)_3 \tag{5}$$

$$2Al(OH)_3 \rightarrow 2AlO(OH) + 2H_2O \tag{6}$$

$$HCHO + O_2 + 2OH^- \rightarrow CO_3^{2-} + 2H_2O \tag{7}$$

$$2Al(OH)_3 + 4Cu^{2+} + CO_3^{2-} + 6OH^- \rightarrow Cu_4Al_2(OH)_{12}CO_3 \tag{8}$$

$$2AlO(OH) + 4Cu^{2+} + CO_3^{2-} + 6OH^- + 2H_2O \rightarrow Cu_4Al_2(OH)_{12}CO_3 \tag{9}$$

Scheme 1. Fabrication process of flower-like MnO$_2$@CuAl-CLDHs with peroxidase-like activity.

3.2. Characterization of MnO₂@CuAl-CLDHs

The morphologies of CuAl-LDHs, CuAl-CLDHs, and MnO$_2$@CuAl-CLDHs were detected by FESEM. As shown in Figure 1a,b, CuAl-LDHs were flower-like microspheres with a size of 4.5 µm and contained numerous interconnected hydroxide nanosheets. The mean thickness of the 2D nanosheets was about 55 nm. The low magnification SEM image (Figure 1a) indicated that the CuAl-LDHs precursors could be synthesized in large quantities. After annealing, the flower-like morphology of CuAl-LDHs was well preserved, while the nanosheets became thinner and the thickness was 33.3 nm due to the shrinkage

caused by the escape of CO_3^{2-} and water (Figure 1c). After the growth of MnO_2 on CuAl-CLDHs surface, the edges of MnO_2@CuAl-CLDHs were much rougher owing to the edge-to-face stacking of ultrathin MnO_2 nanosheets (Figure 1d,e). The self-assembly 3D hierarchical construction possessed abundant channels and higher specific surface area, which were conducive to the adsorption of substrate molecules and the exposure of metal active sites, and ultimately enhanced the catalytic performance of TMB. The TEM image displayed that the center was almost opaque due to the dense accumulation of CuAl-CLDHs, while the ultrathin MnO_2 nanosheets at the edges were transparent, which further confirmed the 3D hierarchical construction of MnO_2@CuAl-CLDHs (Figure 1f). In addition, the EDS mapping was provided to verify the composition of MnO_2@CuAl-CLDHs. As displayed in Figure 1g–k, the Al, Cu, Mn, and O elements were evenly distributed over the entire MnO_2@CuAl-CLDHs. The coexistence of copper ions and manganese ions could provide bimetallic active sites, and the Cu^+/Cu^{2+} and Mn^{3+}/Mn^{4+} redox couples would enhance the nanozyme catalytic activity of MnO_2@CuAl-CLDHs by accelerating the electron transfer rate between TMB and H_2O_2.
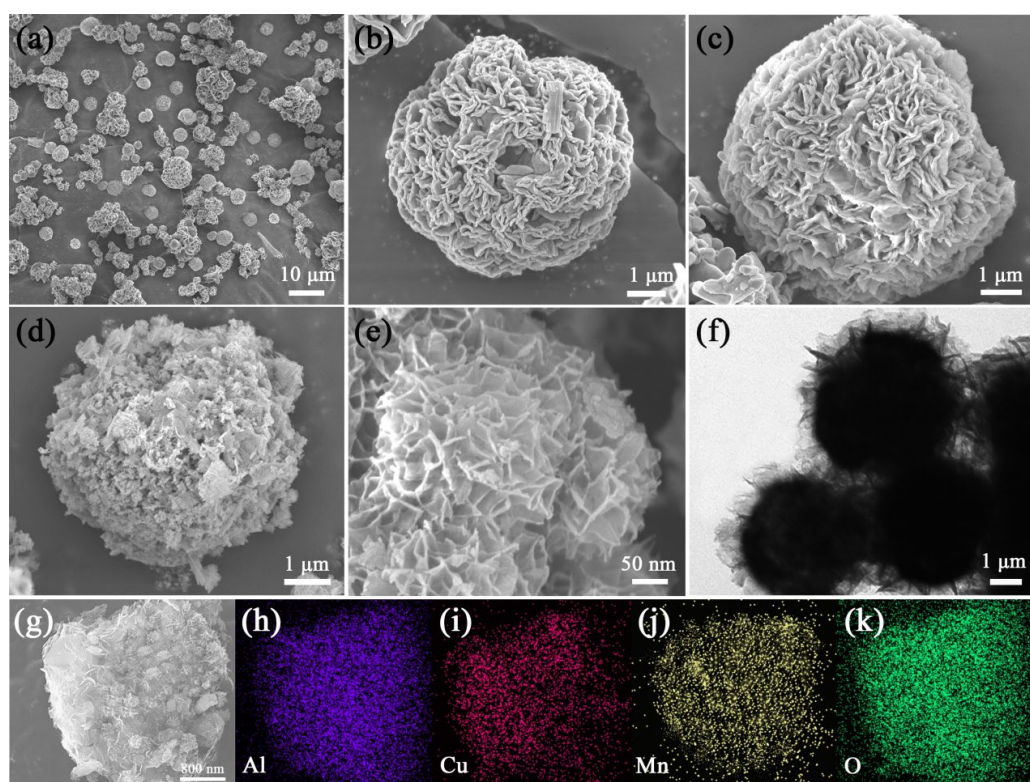
Figure 1. SEM images of (**a**,**b**) CuAl-LDHs, (**c**) CuAl-CLDHs, (**d**,**e**) MnO_2@CuAl-CLDHs. (**f**) TEM image of MnO_2@CuAl-CLDHs. (**g**–**k**) EDS mapping images of MnO_2@CuAl-CLDHs.

The crystal structures of CuAl-LDHs, CuAl-CLDHs, and MnO_2@CuAl-CLDHs were verified by X-ray diffraction (XRD) patterns. The obtained diffraction patterns of the synthesized products were compared with standard PDF cards. PDF cards are standardized diffraction data for phase identification of crystalline materials and are included and published by the International Center for Diffraction Data (ICDD). As shown in Figure 2a, the diffraction peaks at 10.02°, 20.08°, 33.61°, 39.93°, 44.86°, and 60.83° were attributed to (003), (006), (012), (015), (0.18), and (110) planes of CuAl-LDHs (PDF#37-0630). After calcination, the peaks located at 35.42°, 38.66°, 48.73°, 53.47°, 58.22°, 61.54°, 65.73°, and 68.01° belonged to (002), (111), (20-2), (020), (202), (11-3), (022), and (220) planes of CuO (PDF#48-1548). In addition, the diffraction peaks related to Al_2O_3 were observed at 32.41° and 46.28°, which corresponded to the (108) and (2110) planes (PDF#47-1770). The additional diffraction peaks in the XRD pattern of MnO_2@CuAl-CLDHs at 21.18°, 34.14°, and

38.04° originated from the (101), (301), and (111) crystal planes of MnO_2 (PDF#42-1316). No other diffraction peaks were observed, confirming the $MnO_2@CuAl$-CLDHs had been successfully synthesized.
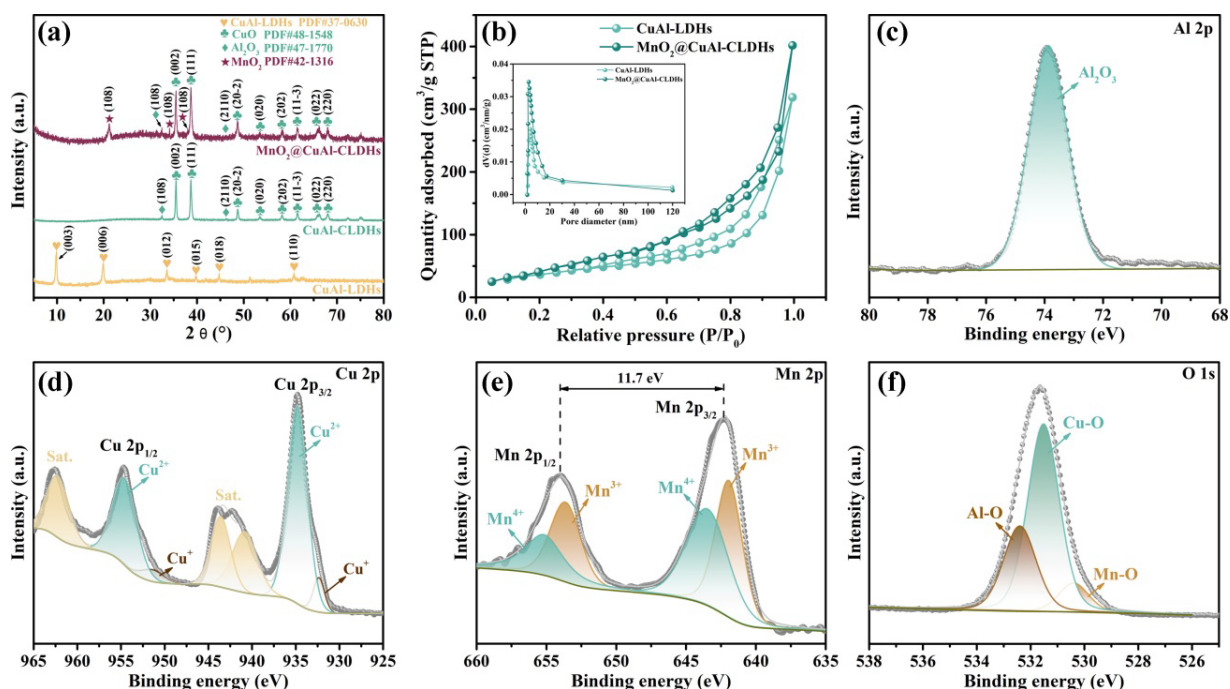
Figure 2. (**a**) XRD spectrum of CuAl-LDHs, CuAl-CLDHs, and $MnO_2@CuAl$-CLDHs. (**b**) N_2 adsorption-desorption and pore size distribution for CuAl-LDHs and $MnO_2@CuAl$-CLDHs. High-resolution XPS spectra of (**c**) Al 2p, (**d**) Cu 2p, (**e**) Mn 2p, and (**f**) O 1s for $MnO_2@CuAl$-CLDHs.

The N_2 adsorption-desorption isotherms of CuAl-LDHs and $MnO_2@CuAl$-CLDHs and the corresponding pore size distribution curves were revealed in Figure 2b, which indicated the multi-order pore structure of flower-like $MnO_2@CuAl$-CLDHs. The N_2 adsorption-desorption isotherms of CuAl-LDHs and $MnO_2@CuAl$-CLDHs all exhibited type-IV isotherms with an H3 hysteresis loop according to the IUPAC classification, indicating the existence of mesoporous structures. The adsorption and desorption isotherms of CuAl-LDHs did not coincide completely and displayed an obvious hysteresis, which was attributed to the presence of macroporous structures [26]. After a coating with MnO_2 nanosheets, the hysteretic loop of $MnO_2@CuAl$-CLDHs reduced, owing to some large pores being filled with MnO_2 nanosheets. However, the N_2 adsorption performance of $MnO_2@CuAl$-CLDHs was improved compared with CuAl-LDHs, which might be because the MnO_2 loading further improved the porosity of the $MnO_2@CuAl$-CLDHs and eventually formed hierarchical pore structures. The pore size distribution curves of $MnO_2@CuAl$-CLDHs showed hierarchical pore structures with abundant micropores and mesopores, which could enhance the performance of catalysts. The specific surface area, pore size, and pore volume of as-prepared samples were listed in Table 1. The specific surface area and pore volume of $MnO_2@CuAl$-CLDHs were 245.4 m^2/g and 0.694 mL/g, respectively, which were higher than those of CuAl-LDHs (167.8 m^2/g and 0.521 mL/g). The abundant pores could accelerate the diffusion of substrate molecules on the surface of catalysts, and the high specific surface area could fully expose the Mn/Cu active sites. The synergistic effect of both sides made the $MnO_2@CuAl$-CLDHs possess excellent catalytic activity.

Table 1. Specific surface area and pore volume of as-synthesized samples.

| Sample	S_{BET} (m^{2}g^{-1})	V_{Total} (cm^{3}g^{-1})	D_p (nm)
CuAl-LDHs	167.8	0.521	3.712
MnO$_2$@CuAl-CLDHs	245.4	0.694	2.831

The chemical composition and elemental states of MnO$_2$@CuAl-CLDHs were examined by X-ray photoelectron spectroscopy (XPS). The as-prepared MnO$_2$@CuAl-CLDHs contained the four elements of Al, Cu, Mn, and O. As shown in Figure 2c, the peak of Al 2p spectrum located at 73.9 eV was assigned to the aluminum oxide (Al$_2$O$_3$) [27,28]. Figure 2d shows the fitting curves of Cu 2p, and the peaks that occurred at 934.8 and 954.7 eV belonged to Cu 2p$_{3/2}$ and Cu 2p$_{1/2}$, respectively. According to the fitting results, the peaks at 932.3 and 951.3 eV were attributed to Cu$^+$, while the peaks at 934.8 and 954.7 eV corresponded to Cu^{2+}. In addition, the binding energies of 940.7, 943.6, and 962.7 eV were ascribed to the Cu^{2+} satellite peaks [29–31]. In Figure 2e, the Mn 2p spectrum was fitting into two peaks located at 642.2 and 653.9 eV, which were ascribed to Mn 2p$_{3/2}$ and Mn 2p$_{1/2}$, respectively. The separation of binding energy between Mn 2p$_{3/2}$ and Mn 2p$_{1/2}$ peaks was 11.7 eV. The fitting peaks at binding energies of 641.9 and 653.6 eV were assigned to Mn^{3+}, while the two peaks located at 643.5 and 655.2 eV were classified as Mn^{4+} [32,33]. Figure 2f displays the O 1s spectra of MnO$_2$@CuAl-CLDHs. The three peaks at binding energies of 530.3, 531.4, and 632.3 eV belonged to Mn-O, Cu-O, and Al-O, respectively [34,35]. The XPS results indicated the coexistence of CuAl-LDHs and MnO$_2$, which was consistent with the XRD analyses, further confirming the successful synthesis of MnO$_2$@CuAl-CLDHs.

3.3. Peroxide-like Activity of MnO$_2$@CuAl-CLDHs

According to reports in the literature, both copper oxides and manganese oxides had excellent nanozyme activity, especially the manganese oxides that possessed peroxidase-like and oxidase-like activities due to the diversity of chemical valence state [36,37]. 3,3′,5,5′-tetramethylbenzidine (TMB) was used as the typical chromogenic substrate to investigate the peroxidase-like activity of MnO$_2$@CuAl-CLDHs. The colorless TMB could be oxidized into blue oxTMB under the catalysis of nanozyme and simultaneously showed a strong absorption signal at 652 nm in the UV-vis spectrum. The oxidases catalyzed TMB oxidation in the presence of O$_2$ (Equation (10)), while the peroxidases realized the catalytic oxidation of TMB with H$_2$O$_2$ as the electron acceptor (Equation (11)).

$$TMB + O_2 \xrightarrow{oxidase} oxTMB + H_2O \tag{10}$$

$$TMB + H_2O_2 \xrightarrow{peroxidase} oxTMB + H_2O \tag{11}$$

As shown in Figure 3a, the absorbance of TMB + H$_2$O$_2$ system (orange curve) at 652 nm was maintained at the initial level (TMB system, green curve), indicating the H$_2$O$_2$ could hardly oxidize TMB solution in the absence of the catalyst. The characteristic absorption peak at 652 nm was witnessed with the addition of CuAl-CLDHs (CuAl-CLDHs + TMB + H$_2$O$_2$ system, brown curve) and MnO$_2$ (MnO$_2$ + TMB + H$_2$O$_2$ system, blue curve), and the chromogenic system became blue, especially for the MnO$_2$ + TMB + H$_2$O$_2$ system, which displayed a higher absorption signal at 652 nm. This suggested that the peroxidase-like activity of MnO$_2$ was higher than that of pure CuAl-CLDHs. In contrast with the MnO$_2$ + TMB + H$_2$O$_2$ system, the reaction system of MnO$_2$@CuAl-CLDHs + TMB + H$_2$O$_2$ (black curve) produced the dark blue solution, indicating that the synthesized MnO$_2$@CuAl-CLDHs displayed the highest catalytic rate and possessed superior peroxidase-like activity due to the synergy between MnO$_2$ and CuAl-CLDHs. Additionally, MnO$_2$@CuAl-CLDHs could also catalyze the oxidation of TMB to produce blue oxTMB in the absence of H$_2$O$_2$ (MnO$_2$@CuAl-CLDHs + TMB system, red curve), which meant MnO$_2$@CuAl-CLDHs also had oxidase-like activity. Therefore, the MnO$_2$@CuAl-CLDHs might possess multiple enzyme-like activities.
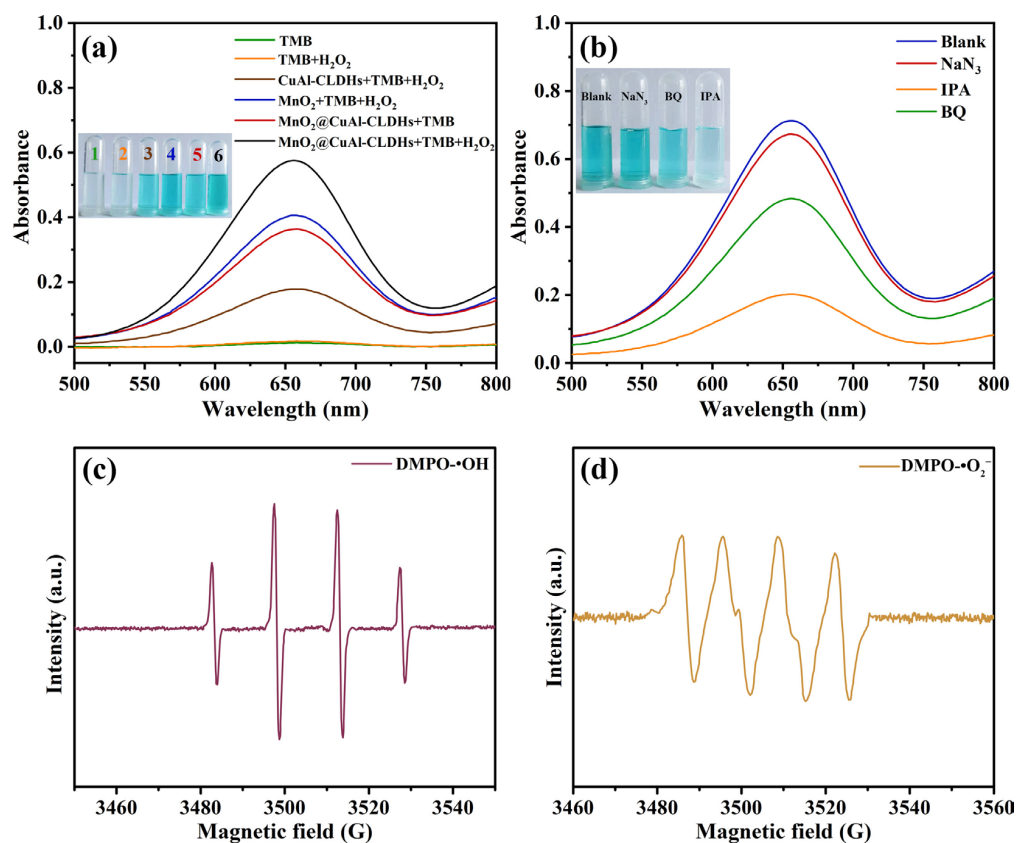
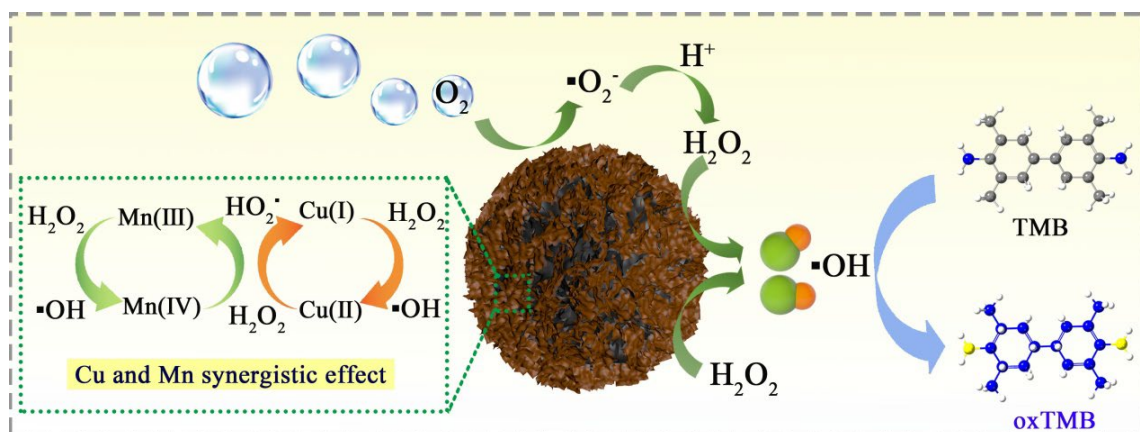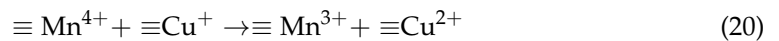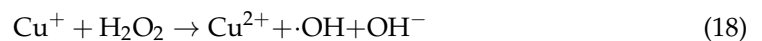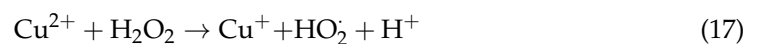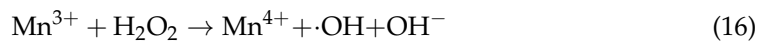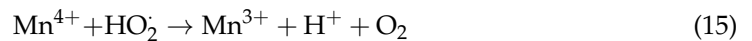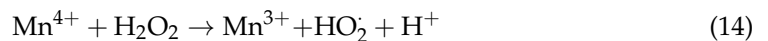**Figure 3.** (**a**) The UV-vis absorption spectra of different reaction systems. (**b**) Effects of various radical scavengers on the colorimetric systems. (**c**,**d**) EPR spectra of DMPO-·OH and DMPO-·O_2^- for MnO_2@CuAl-CLDHs.

3.4. Enzyme-Like Catalysis Mechanism of MnO_2@CuAl-CLDHs

In order to explore the mechanism of the multiple enzyme-like mechanisms of MnO_2@CuAl-CLDHs, IPA, BQ, and NaN_3 were introduced into the chromogenic system to inhibit hydroxyl radicals (·OH), superoxide anions (·O_2^-), and singlet oxygen ($_1O^2$), respectively. As illustrated in Figure 3b, compared with the blank experiment (blue curve), the introduction of IPA (orange curve) significantly inhibited the catalytic activity of the reaction system, while the presence of BQ (green curve) had a weak effect on the absorbance at 652 nm, which reflected that ·OH and ·O_2^- both existed in the chromogenic reaction and ·OH played a vital part. After NaN_3 (red curve) was added to the reaction solution, the color and characteristic absorbance (652 nm) showed negligible variation, revealing that the $_1O^2$ was not the main reactive oxygen species. To further confirm the existence of ·OH and ·O_2^-, the electron paramagnetic resonance (EPR) analysis was performed. As shown in Figure 3c, the characteristic signal of DMPO-·OH with an intensity of 1:2:2:1 was detected, indicating that large amounts of DMPO-·OH were produced in the chromogenic system due to the decomposition of H_2O_2 by MnO_2@CuAl-CLDHs. In addition, as depicted in Figure 3d, four obvious signals of DMPO-·O_2^- (1:1:1:1) could be detected, proving the formation of ·O_2^- during the chromogenic reaction. Therefore, the radical trapping experiment and EPR analyses together confirmed that both ·OH and ·O_2^- were generated, revealing the multiple enzyme-like of MnO_2@CuAl-CLDHs.

The possible catalytic reaction mechanism for the formation of ·OH and ·O_2^- by MnO_2@CuAl-CLDHs with multiple enzyme-like was illustrated in Figure 4. ·OH and ·O_2^- originated from the decomposition of H_2O_2 and reduction of dissolved O_2, respectively. XPS results confirmed the existence of Cu^{2+}, Cu^+, Mn^{4+}, and Mn^{3+}, and the redox couples of Cu^{2+}/Cu^+ and Mn^{4+}/Mn^{3+} provide richer oxidation-reduction reactions. The 3D MnO_2@CuAl-CLDHs had abundant mesoporous and high specific surface area, which

provided rich active sites for the activation of H_2O_2 and O_2. First, the dissolved oxygen was adsorbed on the surface of MnO_2@CuAl-CLDHs, and the Mn^{3+} rapidly transferred electrons to O_2 to produce $\cdot O_2^-$ (Equation (12)). However, the $\cdot O_2^-$ was unstable and further generated H_2O_2 under acidic conditions (Equation (13)), which was in agreement with previous reports [38]. As the typical Lewis base, H_2O_2 directly contacted the Mn^{4+}/Cu^{2+} active site and transferred electrons to transition metal ions, and then the Mn^{4+}/Cu^{2+} obtained electrons from H_2O_2 and turned into Mn^{3+}/Cu^+ (Equations (14) and (17)) [39]. The redox couples of Cu^{2+}/Cu^+ and Mn^{4+}/Mn^{3+} formed a cyclic reaction, which generated a great number of reactive oxygen species ($HO_2\cdot$ and $\cdot OH$) through the decomposition of H_2O_2 by MnO_2@CuAl-CLDHs (Equations (15)–(18)) [40]. Finally, $\cdot OH$ further oxidized TMB to produce blue oxTMB (Equation (19)). Therefore, the established chromogenic system mainly used the peroxide-like activity of MnO_2@CuAl-CLDHs, which was an electron-transfer process from TMB to H_2O_2 using MnO_2@CuAl-CLDHs as the mediator. Separately, Cu(I) could accelerate the cycle between Mn(IV) and Mn(III) due to the standard reduction potential of Cu(II)/Cu(I) (E_0 = 0.16 V) below the Mn(IV)/Mn(III) (E_0 = 0.95 V) (Equation (20)) [41]. Therefore, MnO_2@CuAl-CLDHs showed superior peroxidase-like catalytic activity based on the synergistic effect of Cu and Mn promoting the interfacial electron transfer.

$$Mn^{3+} + O_2 \rightarrow \cdot O_{2-} + Mn^{4+} \tag{12}$$

$$O_{2-} + H^+ \rightarrow H_2O_2 + O_2 \tag{13}$$

$$Mn^{4+} + H_2O_2 \rightarrow Mn^{3+} + HO_2^{\cdot} + H^+ \tag{14}$$

$$Mn^{4+} + HO_2^{\cdot} \rightarrow Mn^{3+} + H^+ + O_2 \tag{15}$$

$$Mn^{3+} + H_2O_2 \rightarrow Mn^{4+} + \cdot OH + OH^- \tag{16}$$

$$Cu^{2+} + H_2O_2 \rightarrow Cu^+ + HO_2^{\cdot} + H^+ \tag{17}$$

$$Cu^+ + H_2O_2 \rightarrow Cu^{2+} + \cdot OH + OH^- \tag{18}$$

$$TMB + \cdot OH \rightarrow H_2O + oxTMB \tag{19}$$

$$\equiv Mn^{4+} + \equiv Cu^+ \rightarrow \equiv Mn^{3+} + \equiv Cu^{2+} \tag{20}$$

Figure 4. The possible mechanism for multiple enzyme-like activity of MnO_2@CuAl-CLDHs.

3.5. Steady-State Kinetic Analysis of MnO_2@CuAl-CLDHs

The steady-state kinetic analysis could further evaluate the catalytic activity of nanozymes. The steady-state kinetic test was carried out with H_2O_2 and TMB as substrates in a suitable concentration range to further evaluate the catalytic activity of nanozymes. Simultaneously, the kinetic parameters of the catalytic oxidation reaction were obtained according to the Michaelis–Menten equation and Lineweaver–Burk plots. As depicted in Figure 5a,c, the reaction rates were positively associated with the substrate concentrations (H_2O_2 and

TMB), and the fitting curves presented good correlativity, indicating that the peroxidase reaction catalyzed by MnO$_2$@CuAl-CLDHs followed the typical Michaelis–Menten behavior. The corresponding kinetic parameters K_m and V_{max} were calculated according to the Lineweaver–Burk plots (Figure 5b,d and Table 2). The K_m of MnO$_2$@CuAl-CLDHs for H$_2$O$_2$ and TMB (0.473 mM and 0.102 mM) was much lower than that of HRP (3.7 mM and 0.43 mM), which revealed a more powerful affinity between MnO$_2$@CuAl-CLDHs and substrates. Furthermore, the K_{cat} values of MnO$_2$@CuAl-CLDHs with TMB and H$_2$O$_2$ as substrates were 0.359 s^{-1} and 0.074 s^{-1}, respectively, which were higher than the reported nanozymes (Table 3). Therefore, MnO$_2$@CuAl-CLDHs possessed higher catalytic efficiency. This might be attributed to the three-dimensional hierarchical MnO$_2$@CuAl-CLDHs having abundant mesopores, which accelerated the adsorption of substrate molecules. Meanwhile, the high specific surface area of MnO$_2$@CuAl-CLDHs exposed more catalytic active sites and the adsorbed substrate molecules quickly reached the exposed active sites for catalytic oxidation. The high affinity of MnO$_2$@CuAl-CLDHs for substrates could improve the sensitivity and reusability of colorimetric sensing and even enable the rapid identification of trace contaminants.
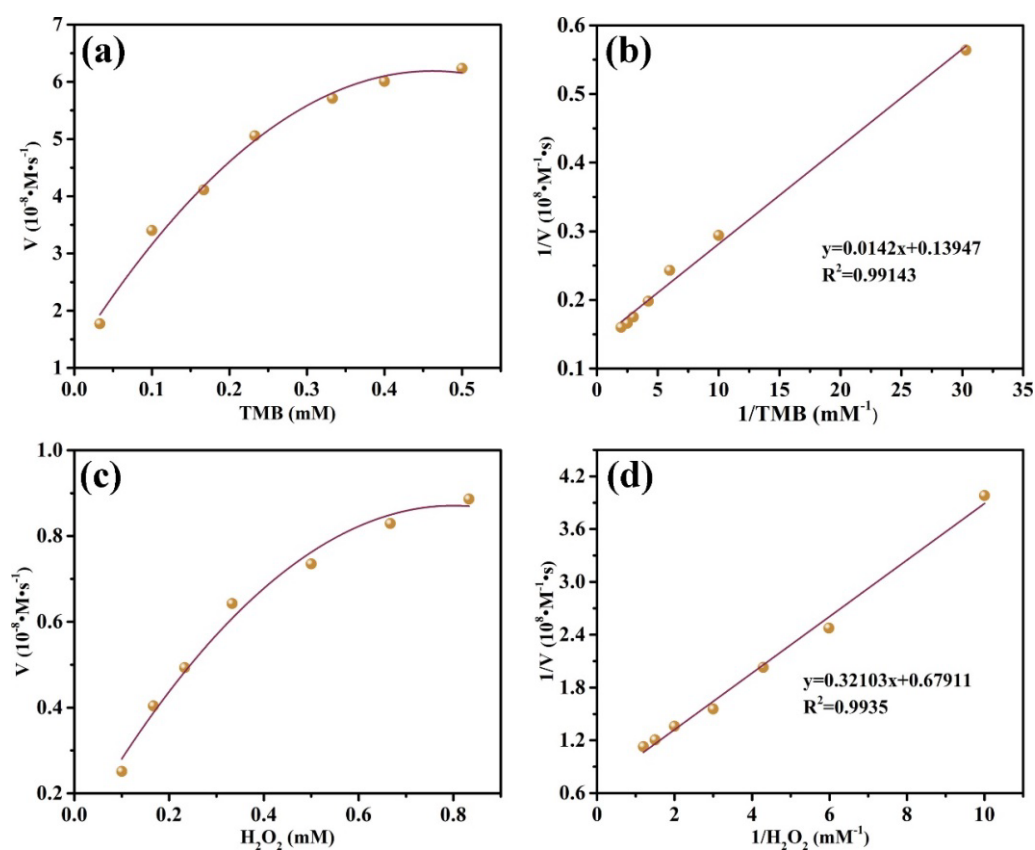
Figure 5. (**a**,**b**) Michaelis–Menten curve and corresponding Lineweaver–Burk plot of MnO$_2$@CuAl-CLDHs for variation of TMB. (**c**,**d**) The Michaelis–Menten curve and corresponding Lineweaver–Burk plot of MnO$_2$@CuAl-CLDHs with H$_2$O$_2$ as substrate.

Table 2. Comparison of the kinetic parameters of MnO$_2$@CuAl-CLDHs and HRP.

Materials	K_m (mM)		V_{max} (10^{-8} M s^{-1})		K_{cat} (s^{-1})		K_{cat}/K_m (s^{-1}·mM^{-1})	
	H$_2$O$_2$	TMB	H$_2$O$_2$	TMB	H$_2$O$_2$	TMB	H$_2$O$_2$	TMB
HRP	3.7	0.43	8.71	10	-	-	-	-
MnO$_2$@CuAl-CLDHs	0.473	0.102	1.473	7.170	0.074	0.359	0.156	3.519

Table 3. Comparison of the catalytic constant (K_{cat}) of different nanozymes.

Nnozymes	K_{cat} (s^{-1}) TMB	K_{cat} (s^{-1}) H_2O_2	Ref.
20CeO$_2$/Y	0.003	0.860	[42]
Cu-N-C	0.283	0.075	[43]
Fe-N-C	0.075	0.073	[44]
Fe$_3$O$_4$-Fe^0/Fe$_3$C	0.680	0.071	[39]
Fe-MOF	0.001	0.0005	[45]
MnO$_2$@CuAl-CLDHs	0.359	0.074	This work

3.6. Optimization of the Catalytic Activity of MnO$_2$@CuAl-CLDHs

The pH value, temperature, and reactant concentration were crucial for the catalytic activity of nanozymes. The reaction conditions of chromogenic system were optimized to obtain the optimum catalytic activity of MnO$_2$@CuAl-CLDHs. Figure 6a displays the absorbance at 652 nm of chromogenic system at different pH values. The best response was obtained at pH 3.0–4.0, indicating that the peroxidase-like activity of MnO$_2$@CuAl-CLDHs reached the optimum under weak-acid conditions. pH 4.0 was chosen for the optimum incubation environment. The color of the reaction system became darker with the extension of time, and the absorbance changed slowly after 9 min (Figure 6b). Therefore, the optimal incubation time was 9 min. The temperature of incubation environment was found crucial for enzymatic activity. As shown in Figure 6c, the enzymatic activity of MnO$_2$@CuAl-CLDHs presented earlier increased and later decreased trend with the increase of incubation temperature, which might be because the high temperature environment accelerated the decomposition of H$_2$O$_2$. The highest absorbance intensities were obtained when the incubation temperature was 30 °C. The concentration of reactants was closely related to the reaction efficiency. Therefore, the effects of TMB, H$_2$O$_2$, and MnO$_2$@CuAl-CLDHs concentrations on the sensing system were investigated. Figure 6d–f showed that the absorbance at 652 nm increased with the increase of reactant concentration and then reached a plateau after the concentration exceeded a certain value, indicating that the reaction efficiency was the highest. Therefore, the optimum concentrations of TMB, H$_2$O$_2$, and MnO$_2$@CuAl-CLDHs were 7 mM, 25 mM, and 1.2 mg/mL, respectively.
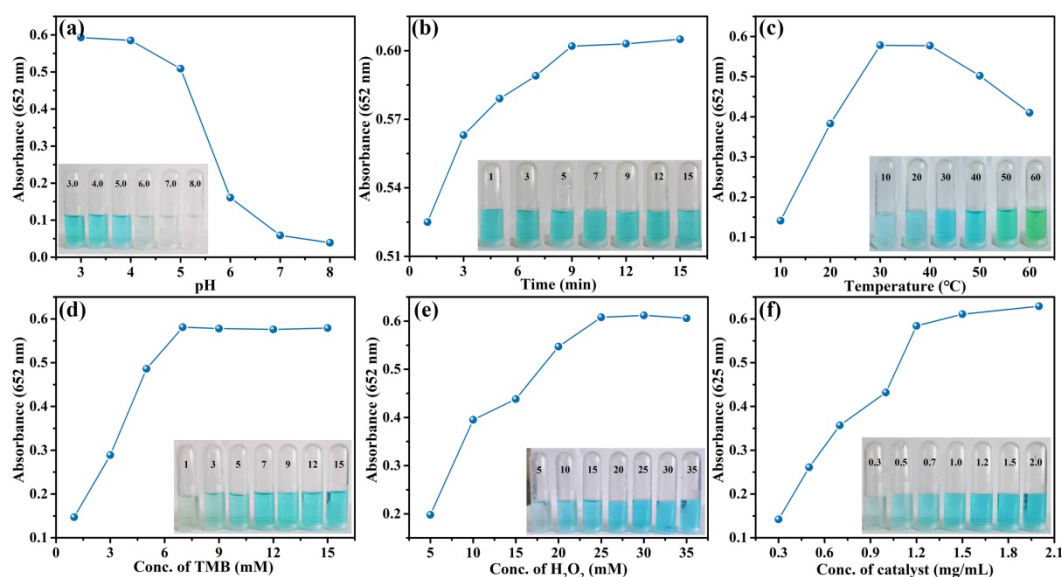
Figure 6. The effect of (**a**) pH, (**b**) reaction time, (**c**) incubation temperature, (**d**) TMB concentrations, (**e**) H$_2$O$_2$ concentrations, and (**f**) catalyst concentrations on the peroxidase-like activity of MnO$_2$@CuAl-CLDHs.

3.7. Colorimetric Detection of HQ

The MnO$_2$@CuAl-CLDHs with excellent peroxidase-like activity were utilized in a colorimetric sensor assay for the determination of HQ under optimal catalytic conditions. As shown in Figure 7a, the signal response at 652 nm gradually decreased with the increase of HQ concentrations and the blue reaction solution gradually became colorless, indicating that the proposed colorimetric platform could realize the determination of HQ by observing the color change of the solution. This visible blue bleaching reaction could be attributed to the double electron reduction between oxTMB and the hydroxyl group on HQ. As displayed in Figure 7b, the concentration of HQ had a linear dependence relation with the absorbance peak at 652 nm in the range of 1–100 μM, and the correlation linear regression equation was y = 0.631983 − 0.00508x (x represents HQ concentration, R^2 = 0.99176) with the detection limit as low as 0.183 μM. Compared with other reported approaches in Table 4, the colorimetric array based on MnO$_2$@CuAl-CLDHs could realize the determination of HQ at lower concentrations in a wide detection range, which indicated the high sensitivity of the established colorimetric sensing platform for HQ.
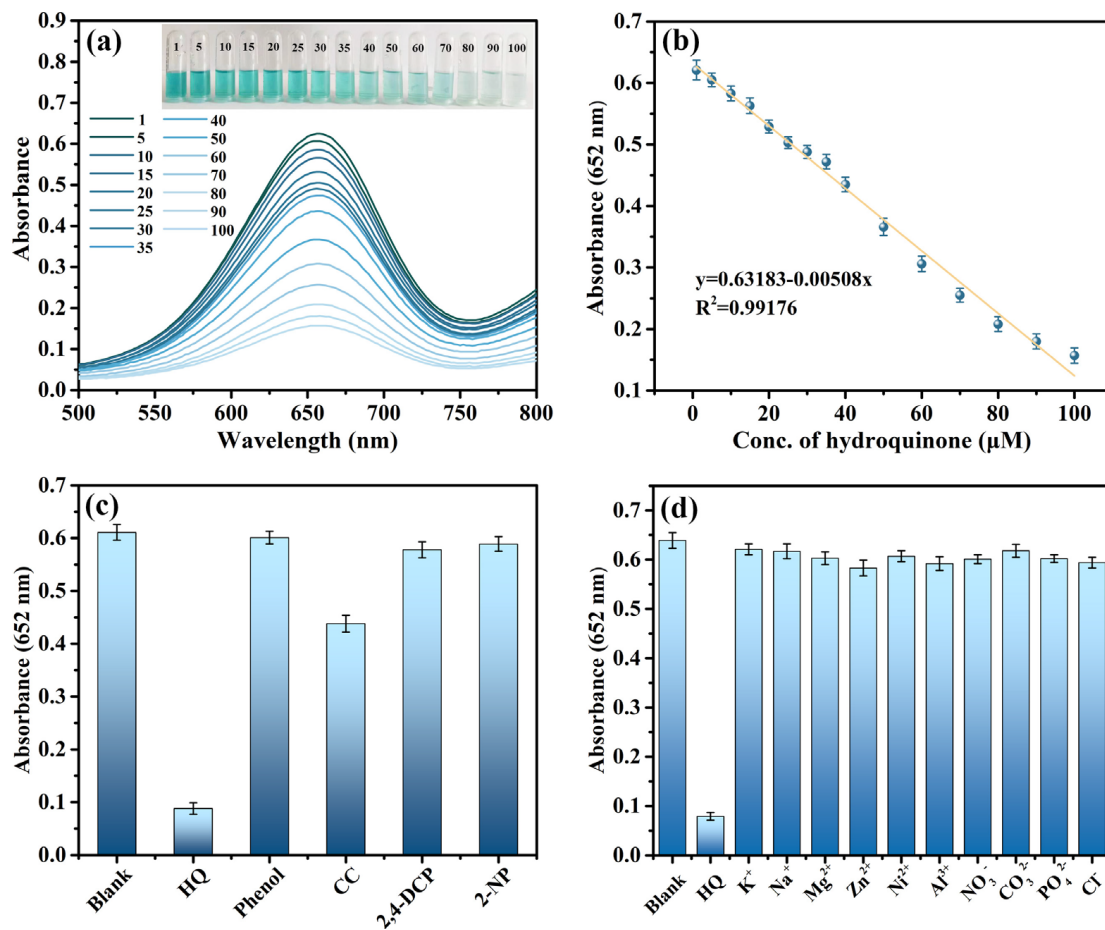

Figure 7. (**a**) The UV-vis absorption spectra of the colorimetric system with the addition of various concentrations of HQ from 1–100 μM. (**b**) The linear calibration plot between absorbance at 652 nm and HQ concentration. (**c**) The selectivity of MnO$_2$@CuAl-CLDHs colorimetric assay to detect HQ (100 μM) by adding an equal amount of phenolic pollutants. (**d**) The anti-interference performance test of the colorimetric sensing system by adding different interference ions.

Table 4. Comparison of the sensing performance with other methods in the detection of HQ.

Sensors	Methods	LOD	Linear Range	Ref.
-	HPLC	0.05 mg/mL	0.2–10 mg/L	[7]
-	AAS	0.039 μg/mL	0.1–25 μg/mL	[5]
Au nanoparticles	colorimetry	0.8 μM	1–30 μM	[46]
$NiMnO_3$	colorimetry	0.68 μM	1–85 μM	[47]
α-Fe_2O_3@CoNi	colorimetry	0.16 μM	0.5–30 μM	[48]
Mn/Fe-MOF@Pd$_{1\cdot0}$	colorimetry	0.09 μM	0.3–30 μM	[49]
CdS/SnS_2	Electrochemistry	0.1 μM	0.2–100 μM	[50]
Fluorescent Polymer Nanoparticles s	Fluorescent	0.21 μM	0–25 μM	[51]
MnO_2@CuAl-CLDHs	colorimetry	0.183	1–100 μM	This work

Selectivity and anti-interference ability were critical for colorimetric assay. Various common interfering ions (K^+, Na^+, Mg^{2+}, Zn^{2+}, Ni^{2+}, Al^{3+}, NO_3^-, CO_3^{2-}, PO_4^{3-}, Cl^-) and phenolic contaminants [phenol, catechol (CC), 2,4-dichlorophenol (2,4-DCP), dinitrophenol (2-NP)] were added into the MnO_2@CuAl-CLDHs+TMB+H_2O_2 system to investigate the anti-interference ability and specificity of MnO_2@CuAl-CLDHs/H_2O_2 colorimetric system for detecting HQ. The concentration of HQ and phenolic contaminants was 100 μM, while that of interfering ions was 10 mM, which was 10-fold the concentration of HQ. As shown in Figure 7c,d, compared to the strong inhibition of HQ to the oxidation of TMB (MnO_2@CuAl-CLDHs + TMB + H_2O_2 + HQ), there was no significant inhibition for the absorbance at 652 nm after introducing high concentrations of interfering ions (MnO_2@CuAl-CLDHs + TMB + H_2O_2 + interfering ions) and the same concentration of phenolic contaminants (MnO_2@CuAl-CLDHs + TMB + H_2O_2 + phenolic contaminants). Only the HQ produced an obvious absorbance response, indicating the strong anti-interference performance and superior specificity of the built colorimetric platform.

The mechanism of HQ detection is presented in Figure 8. The hierarchical mesoporous structure of MnO_2@CuAl-CLDHs provides efficient channels and a larger BET surface area for the adsorption of H_2O_2 and TMB. The way that H_2O_2 converted into ·OH was the Fenton-like reaction with Mn^{4+} and Cu^{2+}. First, the adsorbed H_2O_2 was activated by MnO_2@CuAl-CLDHs to generate ·OH, which oxidized TMB to form blue oxTMB (Equations (11)–(15)). Secondly, two electrons were transferred to blue oxTMB after the introduction of HQ with strong reducibility into the colorimetric system, and the oxTMB was reduced to the colorless TMB. Simultaneously, HQ was oxidized into p-benzoquinone (BQ), resulting in the absorbance signal at 652 nm decreasing gradually as the color of the solution faded. Therefore, the colorimetric array for HQ determination was efficient and sensitive due to the following reasons: (1) The MnO_2@CuAl-CLDHs with high porosity could accelerate substrate diffusion and mass transport. (2) The synergy between larger specific surface area, highly exposed active sites, and the bimetallic active center (Mn^{4+} and Cu^{2+}) further enhanced the peroxidase-like activity of MnO_2@CuAl-CLDHs.
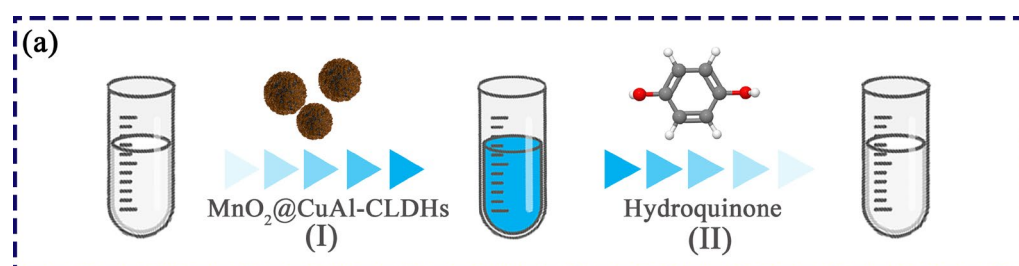
Figure 8. *Cont.*
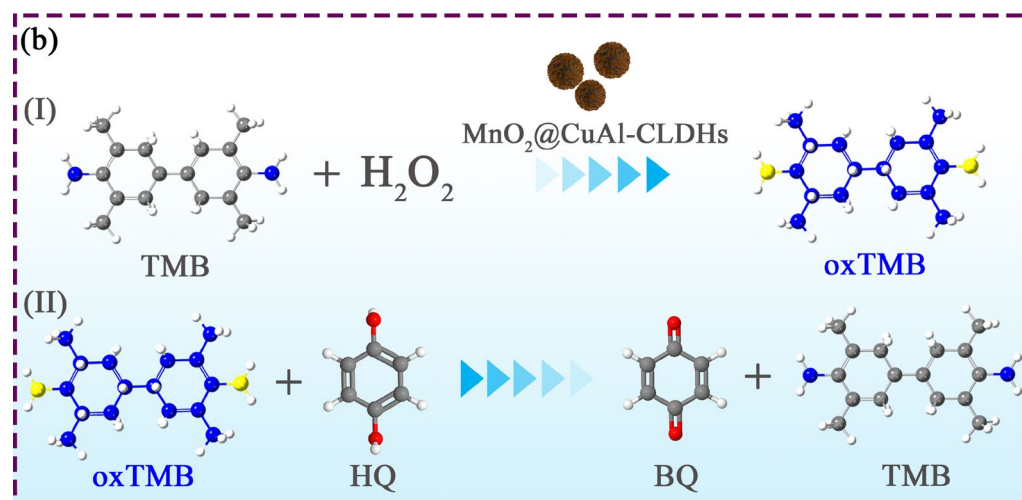
Figure 8. (**a**) The sensing process of colorimetric detection of HQ by MnO$_2$@CuAl-CLDHs. (**b**) The possible mechanism for colorimetric detection of HQ based on MnO$_2$@CuAl-CLDHs.

3.8. Reusability of MnO$_2$@CuAl-CLDHs and Real Sample Analysis

In order to verify the recycling stability of MnO$_2$@CuAl-CLDHs, the circulating experiment of peroxide-like activity was carried out under optimal catalytic conditions. As shown in Figure 9a, the peroxidase-like activity of MnO$_2$@CuAl-CLDHs still maintains 88.7% of the initial activity in the colorimetric system after five cycles of operation, indicating that the synthesized MnO$_2$@CuAl-CLDHs had high stability and reusability. When HQ was added to the colorimetric system, the relative activity of MnO$_2$@CuAl-CLDHs showed slight declines from 15.2% to 4.9% with the increase of the cyclic number, implying the superior reproducibility of MnO$_2$@CuAl-CLDHs-TMB colorimetric assay. The above results showed the characteristics of excellent catalytic activity, high efficiency, and good reproducibility of the established sensor system, which had the potential to apply to the sensitive detection of HQ in real samples. In addition, Figure 9b shows the SEM of MnO$_2$@CuAl-CLDHs-TMB after five successive cycles. The morphology did not change significantly, which was consistent with the initial structure (Figure 1d), indicating that MnO$_2$@CuAl-CLDHs-TMB had higher structural stability.
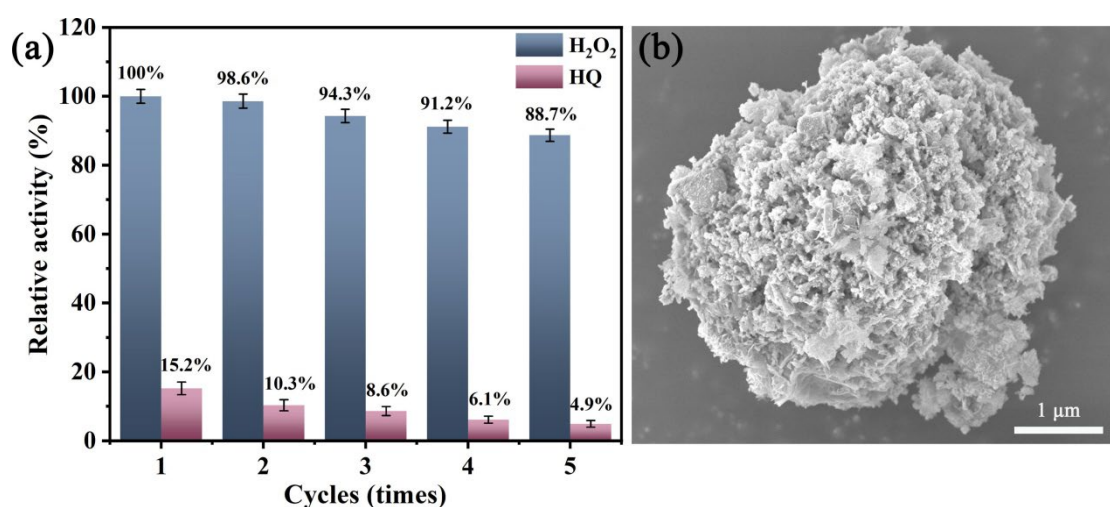
Figure 9. (**a**) The relativity activity (%) of the MnO$_2$@CuAl-CLDHs within five cycles under the optimum conditions. (**b**) SEM image of MnO$_2$@CuAl-CLDHs after use.

To investigate the practical usability of the developed sensor system for HQ determination in real samples, we selected local tap water and lake water as experimental samples

to test the peroxidase-like activity of MnO_2@CuAl-CLDHs. The recovery of HQ in different real samples was determined by standard spike-and-recovery experiment. Table 5 shows that the recoveries in spiked samples ranged from 98.71% to 101.26% with the RSD less than 3%, indicating that the MnO_2@CuAl-CLDHs-TMB colorimetric assay was reliable for monitoring HQ in real water samples.

Table 5. Determination of HQ in real samples using the proposed sensing system.

Sample	Added (μM)	Found (μM)	Recovery (%)	RSD (%, n = 3)
Tap water	5	4.96	99.21	1.01
	30	29.61	98.71	2.15
	60	60.15	100.25	2.07
	80	80.50	100.63	1.91
Lake water	5	4.95	98.91	2.18
	30	29.75	99.18	2.27
	60	60.19	100.31	1.89
	80	81.01	101.26	2.21

4. Conclusions

In summary, 2D MnO_2 nanosheets were constructed in situ on the surface of 3D flower-like CuAl-CLDHs by hierarchical assembly, realizing the integration of high specific surface area with exposed active site and bimetallic active center. The 3D porous structure of CuAl-CLDHs provided abundant attachment sites for MnO_2 nanosheets, and the synthesized MnO_2@CuAl-CLDHs nanozymes exhibited good structural stability and superior peroxide-like activity. A novel colorimetric strategy based on MnO_2@CuAl-CLDHs for HQ detection with high selectivity and high sensitivity was developed, and the detection mechanism was proposed. The established colorimetric assay showed visual detection for HQ ranging from 1 to 100 μM with a detection limit of 0.183 μM. Furthermore, the sensing platform had high anti-interference ability and reusability, which was successfully applied to detect HQ in real water samples. Therefore, the proposed nanozyme-based colorimetric strategy shows potential applications in the analysis of environmental pollutants and the substitutes of natural enzymes by nanozyme.

Author Contributions: Conceptualization, N.X.; methodology, N.X. and L.Y.; formal analysis, X.S., M.Z. and L.W.; investigation, W.T., N.X. and Y.L.; writing—original draft preparation, N.X. and H.Z.; writing—review and editing, W.T. and J.Y.; project administration, W.T.; funding acquisition, W.T. and J.Y. All authors have read and agreed to the published version of the manuscript.

Institutional Review Board Statement: Not applicable.

Informed Consent Statement: Not applicable.

Data Availability Statement: Data are contained within the article.

Conflicts of Interest: The author L.Y. was employed by Shandong Jiazihu New Material Technology Co., Ltd. The remaining authors declare that no conflicts of interest.

References

1. Ahmed, J.; Rahman, M.M.; Siddiquey, I.A.; Asiri, A.M.; Hasnat, M.A. Efficient hydroquinone sensor based on zinc, strontium and nickel based ternary metal oxide (TMO) composites by differential pulse voltammetry. *Sens. Actuators B* **2018**, *256*, 383–392. [CrossRef]
2. Wang, H.; Li, R.; Li, Z. Nanohybrid of Co_3O_4 and histidine-functionalized graphene quantum dots for electrochemical detection of hydroquinone. *Electrochim. Acta* **2017**, *255*, 323–334. [CrossRef]

3. Liang, N.; Ge, X.; Zhao, Y.; Xia, L.; Song, Z.-L.; Kong, R.-M.; Qu, F. Promoting sensitive colorimetric detection of hydroquinone and Hg^{2+} via ZIF-8 dispersion enhanced oxidase-mimicking activity of MnO_2 nanozyme. *J. Hazard. Mater.* **2023**, *454*, 131455. [CrossRef] [PubMed]

4. Huang, L.; Cao, Y.; Diao, D. Electrochemical activation of graphene sheets embedded carbon films for high sensitivity simultaneous determination of hydroquinone, catechol and resorcinol. *Sens. Actuators B* **2020**, *305*, 127495. [CrossRef]

5. Esteki, M.; Nouroozi, S.; Shahsavari, Z. A fast and direct spectrophotometric method for the simultaneous determination of methyl paraben and hydroquinone in cosmetic products using successive projections algorithm. *Int. J. Cosmet. Sci.* **2016**, *38*, 25–34. [CrossRef]

6. Butwong, N.; Kunawong, T.; Luong, J.H.T. Simultaneous Analysis of Hydroquinone, Arbutin, and Ascorbyl Glucoside Using a Nanocomposite of Ag@AgCl Nanoparticles, Ag_2S Nanoparticles, Multiwall Carbon Nanotubes, and Chitosan. *Nanomaterials* **2020**, *10*, 1583. [CrossRef] [PubMed]

7. Marrubini, G.; Calleri, E.; Coccini, T.; Castoldi, A.F.; Manzo, L. Direct Analysis of Phenol, Catechol and Hydroquinone in Human Urine by Coupled-Column HPLC with Fluorimetric Detection. *Chroma* **2005**, *62*, 25–31. [CrossRef]

8. Wang, H.; Wang, X.; Liang, M.; Chen, G.; Kong, R.-M.; Xia, L.; Qu, F. A Boric Acid-Functionalized Lanthanide Metal–Organic Framework as a Fluorescence "Turn-on" Probe for Selective Monitoring of Hg^{2+} and CH_3Hg^+. *Anal. Chem.* **2020**, *92*, 3366–3372. [CrossRef] [PubMed]

9. Xue, Y.; Li, H.; Wu, T.; Zhao, H.; Gao, Y.; Zhu, X.; Liu, Q. Pt deposited on sea urchin-like $CuCo_2O_4$ nanowires: Preparation, the excellent peroxidase-like activity and the colorimetric detection of sulfide ions. *J. Environ. Chem. Eng.* **2022**, *10*, 107228. [CrossRef]

10. Guo, Y.; Wang, H.; Zhang, F.; Xia, J.; Wang, Z. Flexible enzyme cascade sensing platform based on a G-quadruplex nanofiber biohydrogel for target colorimetric sensing. *Anal. Chim. Acta* **2020**, *1140*, 10–17. [CrossRef] [PubMed]

11. Jin, G.; Liu, J.; Wang, C.; Gu, W.; Ran, G.; Liu, B.; Song, Q. Ir nanoparticles with multi-enzyme activities and its application in the selective oxidation of aromatic alcohols. *Appl. Catal. B* **2020**, *267*, 118725. [CrossRef]

12. Sun, L.; Ding, Y.; Jiang, Y.; Liu, Q. Montmorillonite-loaded ceria nanocomposites with superior peroxidase-like activity for rapid colorimetric detection of H_2O_2. *Sens. Actuators B* **2017**, *239*, 848–856. [CrossRef]

13. Yang, W.-P.; Yang, X.; Zhu, L.-J.; Chu, H.-S.; Li, X.-Y.; Xu, W.-T. Nanozymes: Activity origin, catalytic mechanism, and biological application. *Coord. Chem. Rev.* **2021**, *448*, 214170. [CrossRef]

14. Gao, L.; Zhuang, J.; Nie, L.; Zhang, J.; Zhang, Y.; Gu, N.; Wang, T.; Feng, J.; Yang, D.; Perrett, S.; et al. Intrinsic peroxidase-like activity of ferromagnetic nanoparticles. *Nat. Nanotechnol.* **2007**, *2*, 577–583. [CrossRef] [PubMed]

15. Yang, L.; Xu, X.; Song, Y.; Huang, J.; Xu, H. Research progress of nanozymes in colorimetric biosensing: Classification, activity and application. *Chem. Eng. J.* **2024**, *487*, 150612. [CrossRef]

16. Chen, Z.-J.; Huang, Z.; Sun, Y.-M.; Xu, Z.-L.; Liu, J. The Most Active Oxidase-Mimicking Mn_2O_3 Nanozyme for Biosensor Signal Generation. *Chem.-A Eur. J.* **2021**, *27*, 9597–9604. [CrossRef] [PubMed]

17. Jiao, L.; Wu, J.; Zhong, H.; Zhang, Y.; Xu, W.; Wu, Y.; Chen, Y.; Yan, H.; Zhang, Q.; Gu, W.; et al. Densely Isolated FeN_4 Sites for Peroxidase Mimicking. *ACS Catal.* **2020**, *10*, 6422–6429. [CrossRef]

18. Tao, L.; Qiao, M.; Jin, R.; Li, Y.; Xiao, Z.; Wang, Y.; Zhang, N.; Xie, C.; He, Q.; Jiang, D.; et al. Bridging the Surface Charge and Catalytic Activity of a Defective Carbon Electrocatalyst. *Angew. Chem. Int. Ed.* **2019**, *58*, 1019–1024. [CrossRef] [PubMed]

19. Takahashi, Y.; Uchida, H.; Kameda, T.; Kumagai, S.; Saito, Y.; Mizushina, K.; Itou, I.; Han, T.; Yoshioka, T. Synthesis of MnO_2/Mg-Al layered double hydroxide and evaluation of its NO-removal performance. *J. Alloys Compd.* **2021**, *867*, 159038. [CrossRef]

20. Li, M.; Zhou, M.; Wen, Z.Q.; Zhang, Y.X. Flower-like NiFe layered double hydroxides coated MnO_2 for high-performance flexible supercapacitors. *J. Energy Storage* **2017**, *11*, 242–248. [CrossRef]

21. Zhong, M.; Li, X.; Chu, X.; Gui, H.; Zuo, S.; Yao, C.; Li, Z.; Chen, Y. Solar driven catalytic conversion of cellulose biomass into lactic acid over copper reconstructed natural mineral. *Appl. Catal. B* **2022**, *317*, 121718. [CrossRef]

22. Xu, C.; Dong, S.; Chen, T.; Liu, H.; Zou, X.; Ji, M.; Han, Z.; Shu, D.; Wang, C.; Chen, D. Low-temperature catalytic performance of toluene oxidation over Cu-Mn oxide catalysts derived from LDH precursor. *Fuel* **2023**, *347*, 128401. [CrossRef]

23. Asif, M.; Aziz, A.; Wang, Z.; Ashraf, G.; Wang, J.; Luo, H.; Chen, X.; Xiao, F.; Liu, H. Hierarchical CNTs@CuMn Layered Double Hydroxide Nanohybrid with Enhanced Electrochemical Performance in H_2S Detection from Live Cells. *Anal. Chem.* **2019**, *91*, 3912–3920. [CrossRef] [PubMed]

24. Wang, Y.; Yang, D.; Li, S.; Zhang, L.; Zheng, G.; Guo, L. Layered copper manganese oxide for the efficient catalytic CO and VOCs oxidation. *Chem. Eng. J.* **2019**, *357*, 258–268. [CrossRef]

25. Luo, M.; Cheng, Y.; Peng, X.; Pan, W. Copper modified manganese oxide with tunnel structure as efficient catalyst for low-temperature catalytic combustion of toluene. *Chem. Eng. J.* **2019**, *369*, 758–765. [CrossRef]

26. Hao, M.; Gao, P.; Yang, D.; Chen, X.; Xiao, F.; Yang, S. Highly efficient adsorption behavior and mechanism of Urea-Fe_3O_4@LDH for triphenyl phosphate. *Environ. Pollut.* **2020**, *267*, 114142. [CrossRef] [PubMed]

27. Yoon, K.H.; Kim, H.; Koo Lee, Y.-E.; Shrestha, N.K.; Sung, M.M. UV-enhanced atomic layer deposition of Al_2O_3 thin films at low temperature for gas-diffusion barriers. *RSC Adv.* **2017**, *7*, 5601–5609. [CrossRef]

28. Wang, F.; Zhang, Y.; Liang, W.; Chen, L.; Li, Y.; He, X. Non-enzymatic glucose sensor with high sensitivity based on Cu-Al layered double hydroxides. *Sens. Actuators B* **2018**, *273*, 41–47. [CrossRef]

29. Liu, Y.; Sun, M.; Yuan, Y.; Wu, Q.; Wang, H.; He, Y.; Lin, Z.; Zhou, F.; Ling, M.; Qian, C.; et al. Accommodation of Silicon in an Interconnected Copper Network for Robust Li-Ion Storage. *Adv. Funct. Mater.* **2020**, *30*, 1910249. [CrossRef]

30. Lyu, L.; Yan, D.; Yu, G.; Cao, W.; Hu, C. Efficient Destruction of Pollutants in Water by a Dual-Reaction-Center Fenton-like Process over Carbon Nitride Compounds-Complexed Cu(II)-CuAlO$_2$. *Environ. Sci. Technol.* **2018**, *52*, 4294–4304. [CrossRef] [PubMed]

31. Li, X.; Kong, W.; Qin, X.; Qu, F.; Lu, L. Self-powered cathodic photoelectrochemical aptasensor based on in situ–synthesized CuO-Cu$_2$O nanowire array for detecting prostate-specific antigen. *Microchim. Acta* **2020**, *187*, 325. [CrossRef] [PubMed]

32. Li, Y.; Zhang, L.; Zhang, Z.; Liu, Y.; Chen, J.; Liu, J.; Du, P.; Guo, H.; Lu, X. MnO$_2$ Nanospheres Assisted by Cysteine Combined with MnO$_2$ Nanosheets as a Fluorescence Resonance Energy Transfer System for "Switch-on" Detection of Glutathione. *Anal. Chem.* **2021**, *93*, 9621–9627. [CrossRef] [PubMed]

33. Wang, M.; Chen, K.; Liu, J.; He, Q.; Li, G.; Li, F. Efficiently Enhancing Electrocatalytic Activity of α-MnO$_2$ Nanorods/N-Doped Ketjenblack Carbon for Oxygen Reduction Reaction and Oxygen Evolution Reaction Using Facile Regulated Hydrothermal Treatment. *Catalysts* **2018**, *8*, 138. [CrossRef]

34. Fang, R.-C.; Sun, Q.-Q.; Zhou, P.; Yang, W.; Wang, P.-F.; Zhang, D.W. High-performance bilayer flexible resistive random access memory based on low-temperature thermal atomic layer deposition. *Nanoscale Res. Lett.* **2013**, *8*, 92. [CrossRef] [PubMed]

35. Capelli, S.; Motta, D.; Evangelisti, C.; Dimitratos, N.; Prati, L.; Pirola, C.; Villa, A. Effect of Carbon Support, Capping Agent Amount, and Pd NPs Size for Bio-Adipic Acid Production from Muconic Acid and Sodium Muconate. *Nanomaterials* **2020**, *10*, 505. [CrossRef] [PubMed]

36. Wu, Q.; He, L.; Jiang, Z.W.; Li, Y.; Cao, Z.M.; Huang, C.Z.; Li, Y.F. CuO nanoparticles derived from metal-organic gel with excellent electrocatalytic and peroxidase-mimicking activities for glucose and cholesterol detection. *Biosens. Bioelectron.* **2019**, *145*, 111704. [CrossRef] [PubMed]

37. Liu, J.; Meng, L.; Fei, Z.; Dyson, P.J.; Zhang, L. On the origin of the synergy between the Pt nanoparticles and MnO$_2$ nanosheets in Wonton-like 3D nanozyme oxidase mimics. *Biosens. Bioelectron.* **2018**, *121*, 159–165. [CrossRef] [PubMed]

38. Zheng, X.; Liu, Z.; Lian, Q.; Liu, H.; Chen, L.; Zhou, L.; Jiang, Y.; Gao, J. Preparation of Flower-like NiMnO$_3$ as Oxidase Mimetics for Colorimetric Detection of Hydroquinone. *ACS Sustain. Chem. Eng.* **2021**, *9*, 12766–12778. [CrossRef]

39. Baye, A.F.; Nguyen, H.T.; Kim, H. Fe^0/Fe$_3$C-assisted Fe$_3$O$_4$ redox sites as robust peroxidase mimics for colorimetric detection of H$_2$O$_2$. *Sens. Actuators B* **2023**, *377*, 133097. [CrossRef]

40. Sun, Y.; Zhou, J.; Liu, D.; Li, X.; Liang, H. Enhanced catalytic performance of Cu-doped MnFe$_2$O$_4$ magnetic ferrites: Tetracycline hydrochloride attacked by superoxide radicals efficiently in a strong alkaline environment. *Chemosphere* **2022**, *297*, 134154. [CrossRef] [PubMed]

41. Su, Y.; Long, Y.; Chen, J.; Zhao, S.; Li, C.; Qu, F.; Han, B.; Zhang, Z.; Zhang, B.-P. In situ synthesis of Tree-branch-like Copper-manganese oxides nanoarrays supported on copper foam as a superior efficiency Fenton-like catalyst for enhanced degradation of 4-chlorophenol. *Appl. Surf. Sci.* **2022**, *593*, 153241. [CrossRef]

42. Cheng, X.; Huang, L.; Yang, X.; Elzatahry, A.A.; Alghamdi, A.; Deng, Y. Rational design of a stable peroxidase mimic for colorimetric detection of H$_2$O$_2$ and glucose: A synergistic CeO$_2$/Zeolite Y nanocomposite. *J. Colloid Interface Sci.* **2019**, *535*, 425–435. [CrossRef] [PubMed]

43. Wu, Y.; Wu, J.; Jiao, L.; Xu, W.; Wang, H.; Wei, X.; Gu, W.; Ren, G.; Zhang, N.; Zhang, Q.; et al. Cascade Reaction System Integrating Single-Atom Nanozymes with Abundant Cu Sites for Enhanced Biosensing. *Anal. Chem.* **2020**, *92*, 3373–3379. [CrossRef] [PubMed]

44. Jiao, L.; Xu, W.; Zhang, Y.; Wu, Y.; Gu, W.; Ge, X.; Chen, B.; Zhu, C.; Guo, S. Boron-doped Fe-N-C single-atom nanozymes specifically boost peroxidase-like activity. *Nano Today* **2020**, *35*, 100971. [CrossRef]

45. Xu, W.; Jiao, L.; Yan, H.; Wu, Y.; Chen, L.; Gu, W.; Du, D.; Lin, Y.; Zhu, C. Glucose Oxidase-Integrated Metal-Organic Framework Hybrids as Biomimetic Cascade Nanozymes for Ultrasensitive Glucose Biosensing. *ACS Appl. Mater. Interfaces* **2019**, *11*, 22096–22101. [CrossRef] [PubMed]

46. Zhang, L.-p.; Xing, Y.-p.; Liu, L.-h.; Zhou, X.-h.; Shi, H.-c. Fenton reaction-triggered colorimetric detection of phenols in water samples using unmodified gold nanoparticles. *Sens. Actuators B* **2016**, *225*, 593–599. [CrossRef]

47. Liu, Y.; Zhou, M.; Cao, W.; Wang, X.; Wang, Q.; Li, S.; Wei, H. Light-Responsive Metal–Organic Framework as an Oxidase Mimic for Cellular Glutathione Detection. *Anal. Chem.* **2019**, *91*, 8170–8175. [CrossRef] [PubMed]

48. Feng, M.; Wen, S.; Chen, X.; Deng, D.; Yang, X.; Zhang, R. Sweetsop-like α-Fe$_2$O$_3$@CoNi catalyst with superior peroxidase-like activity for sensitive and selective detection of hydroquinone. *RSC Adv.* **2021**, *11*, 24065–24071. [CrossRef]

49. Deng, D.; Wang, Y.; Wen, S.; Kang, Y.; Cui, X.; Tang, R.; Yang, X. Metal-organic framework composite Mn/Fe-MOF@Pd with peroxidase-like activities for sensitive colorimetric detection of hydroquinone. *Anal. Chim. Acta* **2023**, *1279*, 341797. [CrossRef] [PubMed]

50. Huang, L.; Wang, C.; Yang, Y.; Wang, Y.; Li, C.; Xie, Y.; Zhao, P.; Fei, J. A light-driven photoelectrochemical sensor for highly selective detection of hydroquinone based on type-II heterojunction formed by carbon nanotubes immobilized in 3D honeycomb CdS/SnS$_2$. *J. Colloid Interface Sci.* **2023**, *643*, 585–599. [CrossRef] [PubMed]

51. Liu, J.; Bao, H.; Liu, C.; Wu, F.; Fu, T. "Turn-on" fluorometric probe for hydroquinone and catechol based on an in situ reaction between protamine sulfate and dihydroxybenzene isomers and the formation of fluorescent polymer nanoparticles. *Sens. Actuators B. Chem.* **2021**, *333*, 129565. [CrossRef]